Research Article | Vol. 28, No. 26 / 21 December 2020 / Optics Express 38480
Optics EXPRESS

Enhancing the dynamic range of deformable mirrors with compression bias

HUY TUONG CAO,[1,2,*] SEBASTIAN W. S. NG,[1,2] MINKYUN NOH,[3,4] AIDAN BROOKS,[5] FABRICE MATICHARD,[3,5] AND PETER J. VEITCH[1,2]

[1]Department of Physics, University of Adelaide, Adelaide, SA 5005, Australia
[2]OzGrav:The ARC Centre of Excellence for Gravitational Wave Discovery, Australia
[3]LIGO Laboratory, Massachusettes Institute of Technology, Cambridge, MA 02139, USA
[4]The University of British Columbia, Vancouver, BC, Canada
[5]LIGO Laboratory, California Institute of Technology, Pasadena, CA 91125 , USA
*huy.cao@adelaide.edu.au

Abstract: We report the design and testing of a compression-biased thermally-actuated deformable mirror that has a dynamic range larger than the limit imposed by pure-bending stress, negligible higher-order-mode scattering, and a linear defocus response and that is vacuum compatible. The optimum design principles for this class of actuator are described and a mirror with 370 mD dynamic range is demonstrated.

1. Introduction

Adaptive optics are a key technology for astronomy, remote sensing, laser machining and increasingly, high precision interferometry [1,2]. Indeed, the Advanced LIGO (aLIGO) and Virgo gravitational wave detectors employ a range of thermally-actuated adaptive optics to increase the detector sensitivity [3–5]. The recent introduction of vacuum-squeezed light sources to the detectors has necessitated further improvement in the mode-matching [6]. Additional active mirrors that are compatible with high vacuum, can be integrated into a 2-stage vibration-isolation suspension system, have higher-order-mode scatter $< 0.4\%$ and can operate 24/7 are required [7].

We have previously highlighted the shortcomings of currently available adaptive mirrors for use in gravitational wave detectors [8]. We also demonstrated a thermally-actuated bimorph mirror that used an off-the-shelf mirror and could produce a defocus of 200 mD with higher-order-mode scattering loss below 0.4%. The maximum defocus of that mirror was limited by the peel strength of the adhesive used to bond the bimorph layers and the tensile stress at the convex surface of the mirror under bending [8].

In this paper we present a new thermally-actuated optic that resolves both of these limitations, resulting in a much larger dynamic range. This improvement was realised by using the shrink-fitting process to capture the optic - a fused-silica mirror here, within an aluminum ring. This process simultaneously applies a bending moment to the mirror, changing its curvature, and a compressive stress that reduces the tensile stress at the convex surface. The curvature of this mirror, which we refer to as a compression-bias mirror (CBM), is varied by adjusting its temperature.

Analytic and finite element analyses of the CBM and the optimisation of its parameters are discussed in Section 2. We then report in Section 3 a proof-of-principle demonstration of a CBM that uses a 50 mm diameter, 6 mm thick mirror. We also show that the change in curvature can be achieved while maintaining a higher-order-mode scattering below 0.04%.

#408921 https://doi.org/10.1364/OE.408921
Journal © 2020 Received 2 Sep 2020; revised 25 Nov 2020; accepted 27 Nov 2020; published 7 Dec 2020

Optics EXPRESS

2. Compression-bias mirror design

The CBM design is shown in Fig. 1. The inner diameter of the annular ring is initially $2\delta r$ smaller than the outer diameter of the mirror. However, since the thermal expansion coefficient of aluminum is larger than that of fused silica, the CBM can be assembled at an elevated temperature. Cooling to ambient temperature results in an interference-fit between the mirror and ring, and applies a compressive load to the barrel of the mirror, which produces an axi-symmetric bending moment due to the axial offset δz. This moment causes the assembly to deform as shown in Fig. 1(a). The optimisation of the actuator geometry is discussed below using analytic and finite-element models.

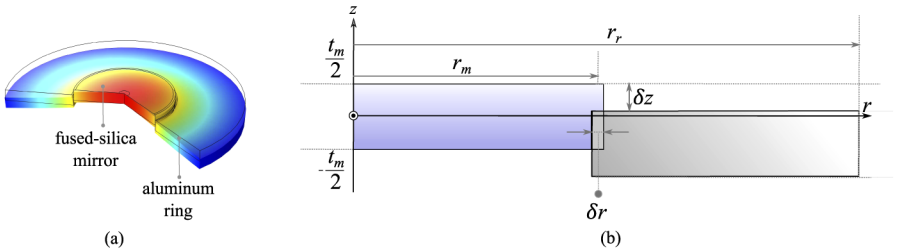

Fig. 1. Schematic of the compression-fit mirror. (*a*): The mirror consists of a fused-silica mirror captured inside an aluminum ring. *b*: The mirror has a radius of r_m and a thickness of t_m. The ring has an inner radius of $r_m - \delta_r$ at room temperature and an outer radius of r_r. δr is also referred to as the radial interference. δz is the axial offset of the aluminum ring upper surface from that of the mirror.

2.1. Analytic model

An analytical model of the CBM is described in Appendix A. It combines ideal plate and thick-wall cylinder theories [9,10] and assumes that the effect of the conical deformation of the aluminum ring is negligible. The predicted curvature of the mirror surface is given by

$$\kappa = \frac{12\beta(\beta-1)(1-\nu_\mathrm{m})(\delta r/r_\mathrm{m})}{t_\mathrm{m}\left[\frac{E_\mathrm{r}}{E_\mathrm{m}}\left(\frac{\rho^2+1}{\rho^2-1}+\nu_\mathrm{r}\right)+(1-\nu_\mathrm{m})\right]} \tag{1}$$

where E_m, E_r, ν_m and ν_r are the Young's modulii and Poisson's ratios of the mirror substrate and the ring. The indices r and m represent the parameters associated with the ring and the mirror respectively. The mirror curvature increases with the ratio of the ring to substrate radii, $\rho = r_\mathrm{r}/r_\mathrm{m}$, however this provides diminishing returns for ring radii larger than twice the substrate radius, as shown in Fig. 3(a). The bending moment of the substrate increases with the ratio of axial offset to substrate thickness, $\beta = \delta z/t_\mathrm{m}$, this moment peaks at an offset ratio of 0.5. Equation (9) predicts that the curvature is independent of ring thickness, t_r. This is a limitation of the thick-wall cylinder analysis that assumes no axial dependence in the contact pressure. Finally, the curvature is seen to increase linearly with the ratio of radial interference to mirror radius, $\delta r/r_m$.

2.2. Finite-element model

A 2D axi-symmetric finite-element (FEM) model of the CBM was implemented in Comsol Multiphysics. It consists of two domains, the fused-silica disk and the aluminum ring, in structural contact. This is a contact problem, which is solved with a slave-master algorithm, in which the domain selected as the slave cannot penetrate the master domain. The choice of master and slave is based on the domain stiffness [11]. In this case, the mirror is the master and the ring is the slave. In the master-slave algorithm, the slave surface discretization must be finer than that

Optics EXPRESS

of the master domain such that the contact force can be computed correctly [12–14]. Thus, the aluminum boundary has a maximum mesh element of 4 μm, which is a factor of 10 smaller than that of the fused-silica boundary, as shown in Fig. 2(a). The material properties and dimensions used in the model are presented in Tables 1 and 2 respectively.

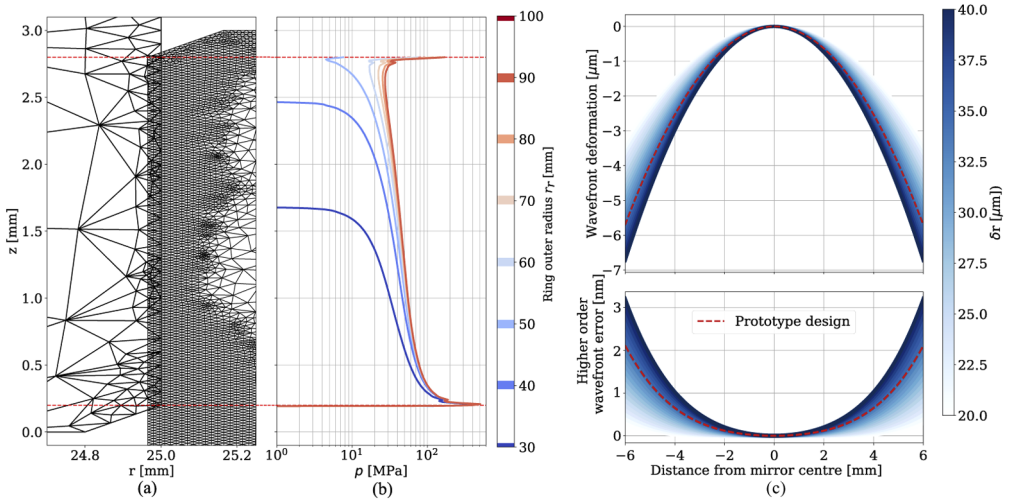

Fig. 2. (a) The FEM meshing at the interface between the substrate and the ring. (b) Interfacial pressure (p) at ambient temperature for various ring outer radius r_r's. The mirror and ring both include a 0.2 mm chamfer. (c) Top panel: predicted mirror deformation at ambient temperature for a range of δr. Bottom panel: non-quadratic component of the deformation. The red-dash curve corresponds to the parameters in Table 2.

The predicted interfacial pressure is plotted in Fig. 2(b) for various r_r's. The average pressure along the interface increases with r_r, as predicted by Eq. (9). The distribution of interfacial pressure is strongly weighted toward the lower edge of the substrate. This means that the compressive force on the mirror far away from the neutral plane is higher than that predicted by thick-wall cylinder theory. This results in greater bending moment estimated by the analytical model.

The FEM predicts a highly-quadratic deformation of the mirror surface. This is plotted for a range of radial interference in Fig. 2(c). The bottom panel shows that the non-quadratic component of the deformation scales linearly with interference and maintains a fractional peak-to-valley aberration below 0.04 % for a 12 mm diameter aperture, which was chosen since the nominal beam radius w in the LIGO optical chain of interest varies between 0.6 and 2 mm [15]. This aperture enables calculation of loss due to higher-order-mode scattering over a $3w$-radius region with negligible clipping losses.

The dependence of the mirror curvature for the key normalised assembly parameters, as predicted by the analytic model and FEM, is plotted in Fig. 3. The FEM confirms that the maximum curvature occurs for an offset ratio ($\delta z/t_m$) of 0.5 and increases with the ratio of ring and mirror radii with diminishing returns above a ratio of 2. Figure 3(c) confirms the discrepancy in the analytical interfacial pressure distribution and indicates an optimal actuator thickness equal to that of the substrate. Finally, the ambient-temperature mirror curvature increases proportionally with $\delta r/r_m$ and the curvature is expected to be 65% larger than predicted by the analytic model. These results indicate that for a given mirror, the actuation ring should have the following properties: $t_r = t_m$, $\delta z = 0.5t_m$ and r_r not significantly greater than $2r_m$ to minimize thermal mass. With these parameters the maximum actuation range is determined by the interference ratio and the resulting stress in the assembly.

Optics EXPRESS

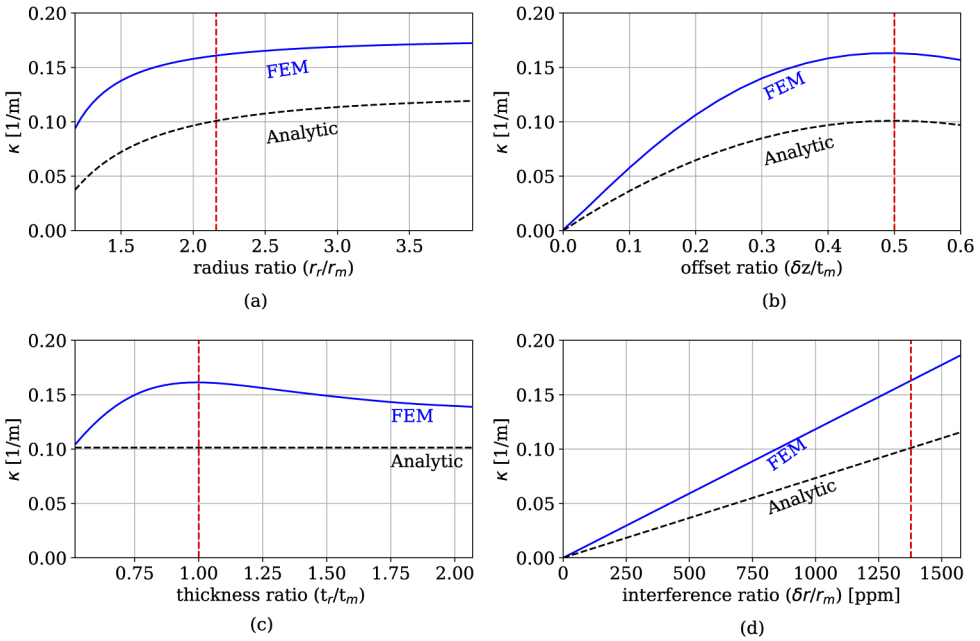

Fig. 3. Dependence of curvature κ on CBM parameters for the analytic and finite-element models. The red-dashed lines correspond to the parameters in Table 2.

2.3. Mechanical stresses

The allowable interference between the mirror and ring is set by the geometry of the mirror and the material strengths. The compressive and shear strength for fused silica can be estimated from Griffith's criteria, giving 430 MPa and 160 MPa respectively [16]. By contrast, the tensile strength varies between 48 and 54 MPa [17–20]. The yield and shear strengths for aluminum 6061-T6 are 275 MPa and 207 MPa, respectively [21]. While stronger aluminum alloys are available, these require compatibility testing for use in the LIGO vacuum.

To determine the effective actuation range, the CBM stress was evaluated in a FEM with the parameters in Table 2. The peak tensile stress in the mirror is shown in Fig. 4(a) and compared with that for a mirror undergoing pure bending [10]. This indicates the maximum allowable curvature of 0.16 m^{-1} in pure bending. The compression bias significantly reduces the maximum tensile stress to 22 MPa stress allowing a safety factor of 2 for this curvature.

The radial and von Mises stress distributions for the mirror and ring at this curvature are shown in Fig. 4(b) and (c). The maximum tensile stress occurs at the mirror front surface and has a proportionality constant of 0.63 MPa/μm of radial interference. The maximum compressive stress on the back surface increases as 2.24 MPa/μm. In the aluminum ring the maximum von Mises stress (σ_v) is 84 MPa, as shown in Fig. 4(b). This is a factor of 3.2 lower Al6061-T6 yield strength, and also increases with δr at a rate of 2.4 MPa/μm. Thus, as expected the compression bias has decreased the tensile stress, enabling a larger δr and actuation range, but increased the compressive stress.

The FEM also predicts stress concentrations in both the mirror and ring, as shown in Fig. 5. In the mirror, the maximum compressive and shear stresses are 360 MPa and 105 MPa respectively, occurring near the back chamfer but not exceeding the material strength. Similarly, there is a stress concentration in the ring near the back contact, with a maximum stress of 420 MPa, which exceeds the yield stress of aluminum 6061-T6. While high stresses are expected near these locations, the magnitudes of these peak stresses increase rapidly as the mesh element size

Optics EXPRESS

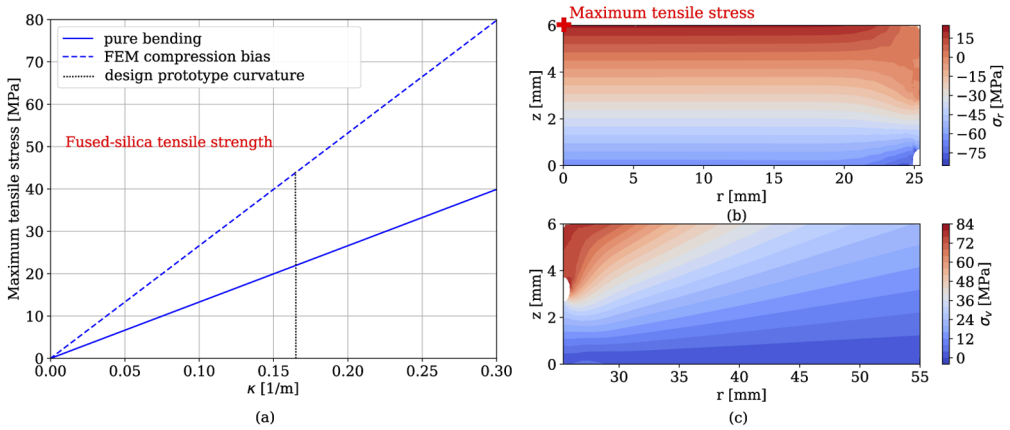

Fig. 4. (a) The maximum front surface tensile stress of the substrate for a given curvature κ. The comparison of pure bending stress and FEM results for the CBM highlight the reduction in maximum tensile stress due to compression bias. A curvature of 0.16 was selected for a prototype mirror corresponding to a safety factor of 2. (b) The corresponding FEM-predicted radial stress in the mirror and (c) von Mises stress in the ring within the assembly at ambient temperature $T = 25°C$ for the mirror parameters specified in Table 2.

is decreased, suggesting the presence of stress singularities in the FEM [22]. Combined with experimental testing these stress singularities may be safely ignored.

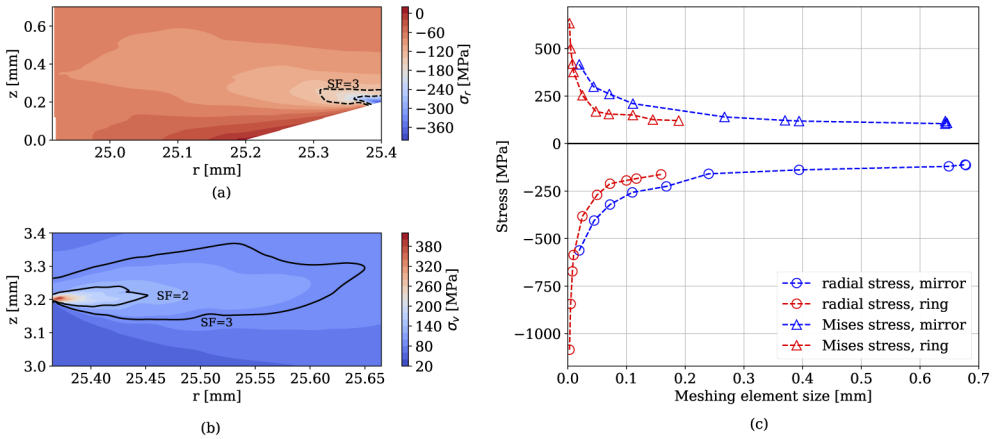

Fig. 5. (a) and (b) shows the concentrations in radial stress occurring in the substrate and von Mises stress in the ring respectively at the rear contact point. (c) shows the dependence of the magnitude of these stresses with the meshing element sizes. This is consistent with the presence of FEM stress singularities.

3. Testing the compression-bias mirror

A 6 mm flat mirror with a nominal figure of $\lambda/10$ was procured and an actuation ring was fabricated according to the parameters in Table 2. The target curvature was 0.16 m^{-1}, for which $\delta r = 36$ μm is required. The CBM was assembled by heating the components to 120°C and using an alignment spacer to provide the desired axial offset and parallelism.

Optics EXPRESS

We describe below three tests of this CBM: measurement of the absolute curvature and figure at ambient temperature, characterisation of its thermal actuation, and a thermal cycling test. The curvature of the CBM was varied by adjusting its temperature, achieved by electrical heating of the actuation ring. To reduce the thermal time constant it is desirable to thermally isolate the ring from its surroundings. Additionally, during actuation the shape of the CBM changes, becoming less conical as its temperature increases, thus it is important that the support does not constrain this change. Mechanical and thermal isolation was achieved by mounting the CBM within a support ring using a thin flexure, as shown in Fig. 6(a). The membrane was conically shaped to increase the natural frequency of the lowest-order normal mode of the mass-loaded membrane.

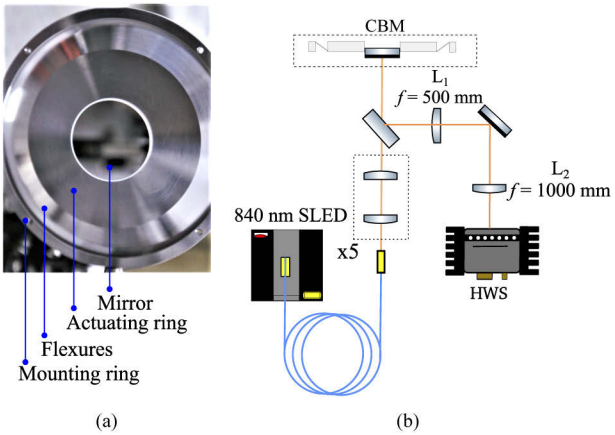

Fig. 6. A schematic of the system used to investigate the thermal actuation of the CBM. A 5× beam expander projects a 840 nm probe beam onto the mirror surface. The wavefront at the mirror surface is imaged onto the Hartmann wavefront sensor (HWS) by the image-relay telescope formed by lenses L_1 and L_2. A photograph of the CBM is shown in the inset.

The curvature measurement approach was similar to that used for the thermal bimorph mirror reported in [8]. Briefly, the mirror is illuminated by an approximately-collimated probe beam from a single-mode-fiber-coupled super-luminescent diode (SLED), as shown in Fig. 6. An image-relay telescope was used to image the wavefront at the mirror onto a Hartmann Wavefront Sensor (HWS) [23], which compared the incident wavefront with a reference wavefront. The HWS system, has as spatial resolution of 215 μm and an accuracy of 0.25 nm_{RMS} [23].

3.1. Curvature and figure test

For this measurement, the reference wavefront was generated by replacing the CBM with a flat mirror and the probe beam was incident with a small, non-zero angle of incidence. The difference wavefront is plotted in Fig. 7(a) and the upper panel of (c).

Wavefront modal analysis [23] yields a spherical power $S = 2\kappa = 374.4 \pm 5.0$ mD, with an astigmatism $C = 12 \pm 7$ mD due to the off-axis angle of incidence. The spherical power corresponds to a radial interference of 39.4 ± 0.6 μm, which is consistent with the nominal interference and the fabrication uncertainty ($\pm 10\mu$m).

A second CBM was assembled with the same stress load and spherical power. This was stored for 6 months at 21°C and no reduction in spherical power was observed. This further indicates that the FEM stress concentrations are not significant.

The deviation from the best-fit S and C quadratics is plotted in Fig. 7(b), with cross sections of the residual wavefront plotted in the lower panel of (c). The RMS residual wavefront error is 5.8 nm over the 5 mm aperture, due mostly to the uncorrelated errors of the mirrors used

Optics EXPRESS

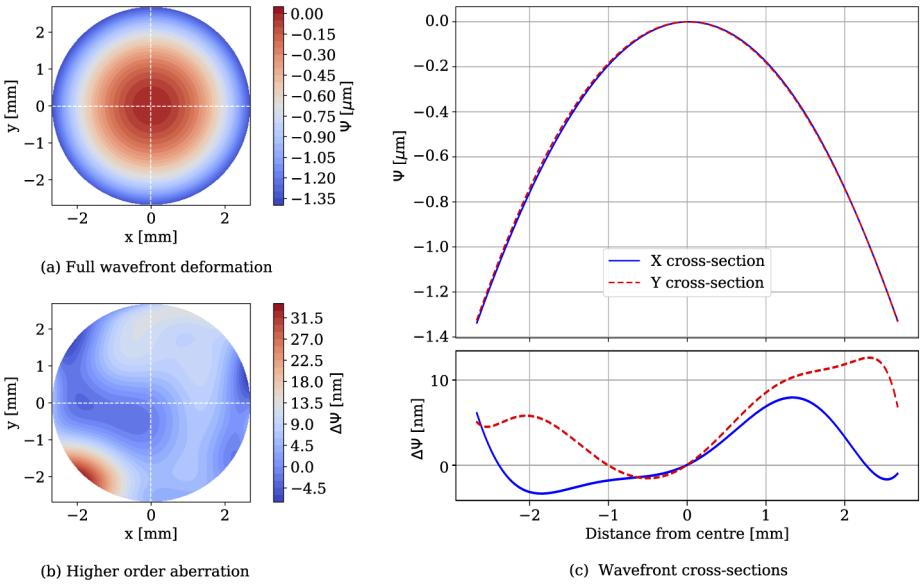

Fig. 7. (a) Measured wavefront at ambient temperature, with cross sections along the white-dashed line plotted in the upper panel of (c). (b) Residual wavefront after removal of the quadratic components, with cross sections along the white-dashed line plotted in the lower panel of (c)

for the reference wavefront and used to produce the CBM. The choice of the aperture size was dictated by the nominal 0.8 mm beam radius at the target position of this deformable mirror in LIGO's output chain, which mode-matches the science beam to the output mode cleaner [24]. The reduced aperture size also allowed us to obtain higher spatial resolution, and thus a more accurate estimation of higher-order-mode scattering loss for the beam size of interest.

The high-order-mode scattering (HOMS) loss is defined as the fraction of power in an incident TEM_{00} mode with a radius w scattered into higher-order modes by calculating the overlap integral between the incident electric field $E_{00}((x - x_o), (y - y_o))$ and the measured residual wavefront map ΔW:

$$\text{HOMS loss}(x_o, y_o) = 1 - \frac{\int E_{00}E_{00}^* e^{-ik\Delta W} dxdy \int E_{00}^* E_{00} e^{ik\Delta W} dxdy}{\left(\int E_{00}E_{00}^* dxdy\right)^2} \tag{2}$$

where (x_o, y_o) represents the center of the TEM_{00} mode, $k = 2\pi/\lambda$ and $\lambda = 1064$ nm.

The HOMS loss was evaluated for a range of beam's position (x_o, y_o) within 1 mm of the centre of the map and using the residual wavefront map appropriate to that location. The results are plotted as a function of w in Fig. 8. It is thus apparent that the CBM easily satisfies the current requirement of HOMS loss < 0.4%, and satisfies the future requirement of 0.04% [24]. Using a mirror with a figure better than $\lambda/10$ would likely result in an even lower scatter loss.

3.2. *Thermal actuation test*

A schematic of the on-axis system used to measure the CBM actuation is shown in Fig. 6. For this measurement, the CBM was heated using four ceramic resistors attached to the actuation ring and it was mounted within a vacuum system to prevent thermal gradients. The wavefront at ambient temperature was used as the reference.

Optics EXPRESS

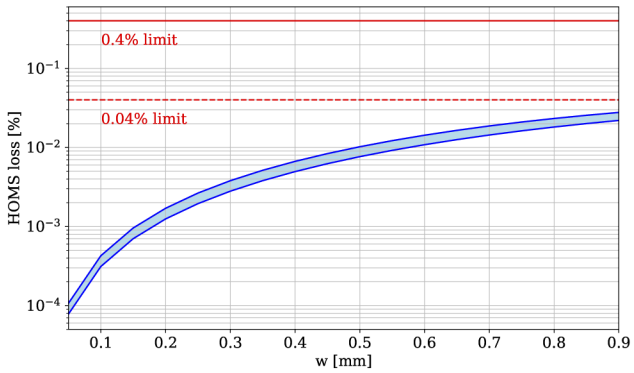

Fig. 8. Higher-order-mode scattering (HOMS) loss for different beam sizes w and the residual wavefront map in Fig. 7(b). The blue band indicates the variation of the loss as the incident beam was moved around the central 2 mm diameter of the map.

The measured spherical and astigmatic powers are plotted as a function of temperature in Fig. 9. The spherical power is linearly dependent on temperature with an actuation constant of

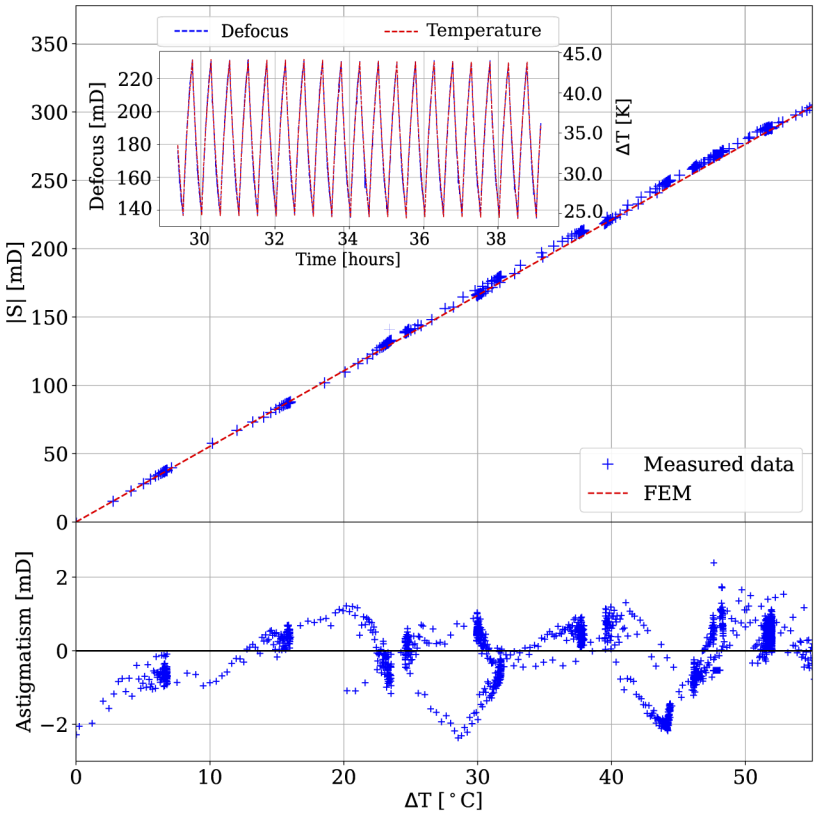

Fig. 9. Plots of the measured change in defocus and the FEM prediction (*top panel*), and astigmatism (*bottom panel*) as a function of change in CBM temperature. *Inset:* The typical temporal variation in temperature and defocus in response to a square-wave heating modulation.

Optics EXPRESS

5.57 mD/K, this agrees with FEM prediction of 5.53 mD/K for $\delta r = 39.4\ \mu$m. The astigmatic power is independent of temperature, implying that it is an artefact of the measurement system.

3.3. Thermal cycling test

A thermal cycling test was conducted to demonstrate dynamic reliability of the CBM and to further mitigate concerns over excess internal stress. During this test, the mirror was cycled 250 times between 45°C and 65°C over 5 days. A plot of some of the data recorded during that test is shown in the inset for Fig. 9. There was no discernible change in the actuation constant during this test.

4. Conclusion

We have presented a deformable mirror that overcomes the tensile stress limit experienced by mirrors in pure bending. This was achieved by applying a compression bias to a commercially available fused silica mirror, doubling the actuation range while maintaining very low higher-order-mode scatter loss. The simple construction of the compression-biased mirror provides ease of integration into seismically isolated suspension systems. The mirror allows reproducible assembly, performance and vacuum compatibility as the assembly does not require adhesive.

We have outlined the key design principles to maximise the actuation range for a given mirror geometry. Following these principles we demonstrated a CBM suitable for active wavefront control in gravitational wave detectors. This was assembled with an off-the-shelf 6 mm thick, 50 mm diameter fused-silica mirror. A maximum defocus of 370 mD, with scatter loss $< 0.04\%$, was achieved at a maximum tensile stress below half the material strength. This dynamic range was tested over 250 cycles and separately at maximum curvature for over 6 months without degradation. Furthermore, the performance of the compression-bias mirror may be readily increased by the reduction of mirror thickness and this technique is suitable for a range of mirror geometries.

Appendix A: analytic model

To determine the optimal geometry of the actuation ring we develop an analytical model of the compression-fit mirror by combining thick-wall cylinder theory and plate theory. The geometry of the compression-bias mirror is defined in Fig. 1(b). The displacements of the substrate and ring boundary are described by the thick-wall cylinder theory:

$$\delta r_r = \frac{r_\mathrm{m} p}{E_\mathrm{r}} \left(\frac{r_\mathrm{r}^2 + r_\mathrm{m}^2}{r_\mathrm{r}^2 - r_\mathrm{m}^2} + \nu_\mathrm{r} \right) \tag{3}$$

$$\delta r_m = \frac{r_\mathrm{m} p}{E_\mathrm{m}} (1 - \nu_\mathrm{m}) \tag{4}$$

where p is the interfacial stress. The sum of each component's deformations is equal to the radial interference $\delta r = \delta r_r + \delta r_m$. Equation (3) and (4) can be rearranged to give an expression for the interfacial stress found in Eq. (5):

$$p = \frac{\delta r}{\frac{r_\mathrm{m}}{E_\mathrm{r}} \left(\frac{r_\mathrm{r}^2 + r_\mathrm{m}^2}{r_\mathrm{r}^2 - r_\mathrm{m}^2} + \nu_\mathrm{r} \right) + \frac{r_\mathrm{m}}{E_\mathrm{m}} (1 - \nu_m)}, \tag{5}$$

The radial and hoop stresses in the mirror and the aluminum ring are also given by the Lamé equations [9]:

Aluminum ring:

$$\sigma_{\mathrm{r,r}} = \sigma_{\phi,\mathrm{r}} = \frac{r_\mathrm{i}^2 p}{r_\mathrm{r}^2 - r_\mathrm{i}^2} \left(1 + \frac{r_\mathrm{r}^2}{r_\mathrm{i}^2} \right) \tag{6}$$

Optics EXPRESS

Fused-silica mirror:

$$\sigma_{\mathrm{r,m}} = \sigma_{\phi,\mathrm{m}} = -p \tag{7}$$

Using Eq. (5), the bending moment on the fused silica is evaluated with plate theory [10]:

$$\begin{aligned} M &= \int_{-t_\mathrm{m}/2}^{t_\mathrm{m}/2} pz dz = p \int_{-t_\mathrm{m}/2}^{t_\mathrm{m}/2-\delta z} z dz \\ &= \frac{p}{2}\delta z\,(\delta_z - t_\mathrm{m}) \end{aligned} \tag{8}$$

in which the origin is at the neutral plane. In plate theory, this neutral plane is assumed to be the mid-plane. Assuming that any deviation of the neutral plane from mid-plane is negligible, the curvature of the mirror front surface is:

$$\kappa = \frac{12\beta(\beta-1)(1-\nu_\mathrm{m})(\delta r/r_\mathrm{m})}{t_\mathrm{m}\left[\frac{E_\mathrm{r}}{E_\mathrm{m}}\left(\frac{\rho^2+1}{\rho^2-1}+\nu_\mathrm{r}\right)+(1-\nu_\mathrm{m})\right]} \tag{9}$$

where D is the flexural rigidity, given by $D = E_\mathrm{m}t^3/(12(1-\nu_\mathrm{m}^2))$, $\beta = \delta z/t_\mathrm{m}$ and $\rho = r_r/r_m$.

In practice, shrink-fitting applies a compression offset to the distribution of stress within the fused-silica disk, shifting the neutral axis upwards. The curvature predicted by Eq. (9) will thus be an underestimation.

Appendix B: actuator parameters

Table 1. Material properties of aluminum alloy 6061-T6 and fused-silica used in modelling the compression-fit mirror [17,21,25]

	Aluminum	Fused silica	
Young's modulus	68.9	73.6	[GPa]
Poisson's ratio	0.33	0.17	
Yield strength	275	54	[MPa]
CTE	23.6	0.57	10^{-6} [1/K]
Heat capacity	896	736	[J/(kg· K)]
Thermal conductivity	167	1.38	[W/(m· K)]

Table 2. Dimensions of the prototype compression-bias mirror with nominal δr = 35 μm.

	Mirror	Actuation ring	Flexure	Support ring	
Inner radius	-	25.4 - δr	55	72.5	[mm]
Outer radius	25.4	55	72.5	80	[mm]
Thickness	6	6	0.3	6	[mm]

Funding

Australian Research Council (CE170100004); National Science Foundation (PHY-0757058).

Acknowledgement

This research was conducted jointly with the support of the Australian Research Council Centre of Excellence for Gravitational Wave Discovery and the National Science Foundation under the LIGO cooperative agreement.

Optics EXPRESS

Disclosures

The authors declare no conflicts of interest.

References

1. R. Davies and M. Kasper, "Adaptive optics for astronomy," Annu. Rev. Astron. Astrophys. **50**(1), 305–351 (2012).
2. P. S. Salter and M. J. Booth, "Adaptive optics in laser processing," Light: Sci. Appl. **8**(1), 110 (2019).
3. R. Lawrence, M. Zucker, P. Fritschel, P. Marfuta, and D. Shoemaker, "Adaptive thermal compensation of test masses in advanced LIGO," Classical Quantum Gravity **19**(7), 1803–1812 (2002).
4. A. F. Brooks, B. Abbott, M. A. Arain, G. Ciani, A. Cole, G. Grabeel, E. Gustafson, C. Guido, M. Heintze, A. Heptonstall, M. Jacobson, W. Kim, E. King, A. Lynch, S. O'Connor, D. Ottaway, K. Mailand, G. Mueller, J. Munch, V. Sannibale, Z. Shao, M. Smith, P. Veitch, T. Vo, C. Vorvick, and P. Willems, "Overview of advanced ligo adaptive optics," Appl. Opt. **55**(29), 8256–8265 (2016).
5. A. Brooks and V. Fafone, *Advanced Interferometric Graviational-Wave Detectors* (World Scientific, 2019), chap. 22: Thermal Adaptive Optics, pp. 609–637.
6. E. Oelker, L. Barsotti, S. Dwyer, D. Sigg, and N. Mavalvala, "Squeezed light for advanced gravitational wave detectors and beyond," Opt. Express **22**(17), 21106–21121 (2014).
7. A. Perreca, A. F. Brooks, J. W. Richardson, D. Töyrä, and R. Smith, "Analysis and visualization of the output mode-matching requirements for squeezing in advanced ligo and future gravitational wave detectors," Phys. Rev. D **101**(10), 102005 (2020).
8. H. T. Cao, A. Brooks, S. W. S. Ng, D. Ottaway, A. Perreca, J. W. Richardson, A. Chaderjian, and P. J. Veitch, "High dynamic range thermally actuated bimorph mirror for gravitational wave detectors," Appl. Opt. **59**(9), 2784–2790 (2020).
9. S. Timoshenko and J. N. Goodier, *Theory of Elasticity* (McGraw-Hill, Inc, 1951), chap. Two-Dimensional Problems in Polar Coordinate, pp. 58–60.
10. S. Timoshenko and J. N. Goodier, *Theory of plates and shells* (McGraw-Hill, Inc, 1959), chap. Pure Bending of Plates, pp. 38–45.
11. COMSOL Multiphyiscs, *Structural Mechanics Module User's Guide* (2017).
12. E. Pichelin, K. Mocellin, L. Fourment, and J.-L. Chenot, "An application of a master-slave algorithm for solving 3d contact problems between deformable bodies in forming processes," Revue Européenne des Éléments Finis **10**(8), 857–880 (2001).
13. A. Habraken and S. Cescotto, "Contact between deformable solids: The fully coupled approach," Math. Comput. Model. **28**(4-8), 153–169 (1998). Recent Advances in Contact Mechanics.
14. P. Hild, "Numerical implementation of two nonconforming finite element methods for unilateral contact," Comput. Methods Appl. Mech. Eng. **184**(1), 99–123 (2000).
15. L. McCuller and L. Barsotti, "Design Requirement Document of the A+ filter cavity and relay optics for frequency dependent squeezing," Tech. Rep. T1800447-v7, LIGO Scientific Collaboration (2020).
16. H. Crandall Stephen, C. Dahl Thomas, and J. Lardner Norman, *Introduction to Mechanics of Solids* (McGraw-Hill, Inc., 1978), chap. 5: Strain-Stress-Temperature Relation, p. 329, 2nd ed.
17. Heraeus Conamic UK Ltd, "Properties of fused silica," (2019).
18. *Corning HPFS 7979, 7980, 8655 Fused Silica.*
19. Tosoh USA Inc., *Fused silica glass* (2013).
20. "Momentive mechanical properties of fused quartz glass," https://www.momentive.com/en-US/categories/quartz/mechanical-properties/#. Accessed: 2019-01-30.
21. ASM Aerospace Specification Metals Inc, "Aluminum 6061-T6; 6061-T651," (2001).
22. G. Sinclair, "Stress singularities in classical elasticity–I: Removal, interpretation, and analysis," Appl. Mech. Rev. **57**(4), 251–298 (2004).
23. A. F. Brooks, T.-L. Kelly, P. J. Veitch, and J. Munch, "Ultra-sensitive wavefront measurement using a hartmann sensor," Opt. Express **15**(16), 10370–10375 (2007).
24. A. F. Brooks, "Design Requirement Document of the A+ Active Wavefront Control Sensors and Actuators," Tech. Rep. E1800480-v1, LIGO Scientific Collaboration (2018).
25. Thorlabs, Inc., "Optical Substrates - UV Fused Silica," (2019).